Opto-Electronics Review

Electro-optical performance and anisotropic transport study of a Ga-free type-II superlattice barrier structure

Maxime Bouschet[1,2*], Vignesh Arounassalame[3], Anthony Ramiandrasoa[3], Jean-Philippe Perez[1],
Nicolas Péré-Laperne[2], Isabelle Ribet-Mohamed[3], Philippe Christol[1]

[1]IES, Université de Montpellier, CNRS, 860 Saint Priest St., F-34000 Montpellier, CEDEX 5, France
[2]LYNRED, BP 21, 364 de Valence Ave., 38113 Veurey-Voroize, France
[3]ONERA, Chemin de la Hunière, F-91761 Palaiseau Cedex, France

Article info	Abstract
	In the past ten years, InAs/InAsSb type-II superlattice has emerged as a promising technology for high-temperature mid-wave infrared photodetector. Nevertheless, transport properties are still poorly understood in this type of material. In this paper, optical and electro-optical measurements have been realised on InAs/InAsSb type-II superlattice mid-wave infrared photodetectors. Quantum efficiency of 50% is measured at 150 K, on the front side illumination and simple pass configuration. Absorption measurement, as well as lifetime measurement are used to theoretically calculate the quantum efficiency thanks to Hovel's equation. Diffusion length values have been extracted from this model ranging from 1.55 µm at 90 K to 7.44 µm at 200 K. Hole mobility values, deduced from both diffusion length and lifetime measurements, varied from 3.64 cm²/Vs at 90 K to 37.7 cm²/Vs at 200 K. The authors then discuss the hole diffusion length and mobility variations within temperature and try to identify the intrinsic transport mechanisms involved in the superlattice structure.

1. Introduction

In the past decade, the infrared detection field has been focused on the emergence of the type-II superlattice (T2SL) technology. Indeed, until now, the InSb and HgCdTe (MCT) infrared photodetectors are the leading technologies in the mid-wave infrared (3–5 µm) spectral range. However, despite high performances reached, InSb and MCT have some limits: for example, InSb suffers from a low Shockley-Read-Hall lifetime, close to 700 ns [1] limiting its operating temperature between 80 K and 90 K. On the other hand, MCT is challenging to manufacture and a few providers can handle it [2]. In this context, strain-balanced InAs/InAsSb T2SL on GaSb substrate, especially combined with a barrier structure design, called XBn [3], seems promising to address some of these limitations. Thus, T2SL takes advantage of GaSb large format substrates, III-V strong uniformity, and the use of the XBn

barrier design allows the reduction of the dark current leading to an enhancement of the operating temperature [4, 5].

Nevertheless, InAs/InAsSb material has two significant disadvantages: being a type-II quantum well structure, the hole and electron are spatially separated, leading to a wave function overlap degradation and, thus, the light absorption reduction in comparison with InSb and MCT bulk material.

Also, InAs/InAsSb is a very anisotropic structure with a great hole confinement along the growth direction generating a very heavy hole mass [6]. Moreover, several experimental studies show very poor hole mobility along the *z*-axis, close to 10 cm²/Vs at 150 K [7], very far from MCT and InSb values, between 100 cm²/Vs and 500 cm²/Vs, respectively [2, 8].

For these two reasons, it was thought for a long time that it would not be possible to reach important performances, particularly in terms of quantum efficiency with Ga-free T2SL materials [9]. However, this technology now demonstrates significant performances with quantum

*Corresponding author at: maxime.bouschet@ies.univ-montp2.fr

efficiency values higher than 50% at 150 K, on a simple pass [4, 10, 11]. In this paper, a focused effort has been invested into the transport properties of minority carriers to explain and understand the performances obtained. The authors then seek to discuss the intrinsic transport mechanisms involved in the superlattice structure.

2. Materials and devices

Based on Ref. 4, two types of heterostructures have been studied [Fig. 1(a)], both grown on n-type GaSb: Te-doped (100) substrates by a 412 Riber molecular beam epitaxy. The first type, called "test sample" allows to focus the authors' study on the InAs/InAsSb T2SL properties, especially for optical absorption and magneto-absorption measurements. Indeed, this test sample consists of a 400 nm GaSb buffer layer, followed by a 3 μm thick layer of an InAs/InAsSb T2SL absorbing layer, and finally capped by a 100 nm GaSb layer. The InAs/InAsSb T2SL is designed with a 35% Sb and with InAs and InAsSb thicknesses of 3.9 nm and 1.3 nm, respectively.
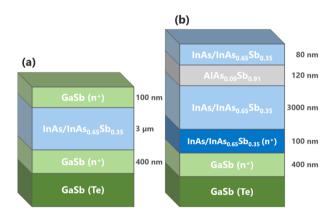

Fig. 1. InAs/InAsSb T2SL heterostructures schematic cross section: test sample structure (a) and barrier structure (b).

The second type of heterostructure is a barrier structure [Fig. 1(b)] composed of a 400 nm GaSb buffer layer, a 100 nm highly doped T2SL InAs/InAs$_{0.65}$Sb$_{0.35}$ bottom contact layer, a 3 μm InAs/InAs$_{0.65}$Sb$_{0.35}$ T2SL absorbing layer, a 120 nm AlAs$_{0.09}$Sb$_{0.91}$ barrier layer, and, finally, capped by a 80 nm InAs/InAs$_{0.65}$Sb$_{0.35}$ T2SL (top contact layer). Residual doping of InAs/InAs$_{0.65}$Sb$_{0.35}$ T2SL layers is determined by capacitance-voltage measurement [12] close to $3 \cdot 10^{15}$ cm^{-3} (n-type) and the one of AlAs$_{0.09}$Sb$_{0.81}$ barrier layer is estimated close to $2 \cdot 10^{16}$ cm^{-3} (p-type). This intrinsic p-type nature of the barrier layer creates a pn-junction with the absorber interface. Thus, a part of the absorber layer is depleted. Therefore, although the dark current is reduced, a generation-recombination (GR) dark current component is still present in this structure. This shows that the design of the structure is not optimized at this time. Nevertheless, it was decided to leave the barrier layer non-intentionally doped with a p-type residual doping since the authors are aware that the accurate n-type doping of AlAsSb is hard to manage. As this point is not discussed in this study, the authors will situate themselves here in the case of an ideal diffusion-limited barrier structure.

The barrier structure is then processed into discrete detectors with diameters ranging from 60 μm to 310 μm using standard photolithography techniques. Deep etching through the total absorber layer is performed to perfectly isolate each photodiode and suppress lateral contribution [13]. Barrier structures are used to perform electrical and electro-optical measurements such as current voltage or quantum efficiency.

3. Measurements

The performances of the authors' devices mainly depend on two figures of merit: electrically, on the dark current diffusion, and electro-optically, on the quantum efficiency. Based on (1) the first one depends on n_i, the intrinsic carrier concentration, the product of the doping level N_D, the minority lifetime τ, the electric charge q, and, finally, on the diffusion length L_D. According to (2), the diffusion length is a function of the minority carrier mobility μ and the minority carrier lifetime τ. On its side, the quantum efficiency mainly depends on α, the absorption coefficient, and L_D, the diffusion length.

$$J_{diffusion} = \frac{q \cdot n_i^2}{N_D \cdot \tau} L_D \qquad (1)$$

$$L_D = \sqrt{\mu\tau\left(\frac{kT}{q}\right)}. \qquad (2)$$

3.1. Lifetime measurements

The authors start with minority carrier lifetime measurements directly performed on barrier structure [Fig. 1(b)] through the time-resolved photoluminescence (TRPL) technique [14].

Fig. 2 shows minority carrier lifetime values measured between 77 K and 260 K. The first regime can be observed, below 200 K, corresponding to a Shockley-Read-Hall (SRH) limited regime, where the lifetime remains almost constant with an approximate value of 1 μs. This value is lower than the one recently reported in the literature for similar Ga-free T2SL [10] but proves the material quality of the grown structure. Above 200 K, the lifetime decreases rapidly, from 1 μs at 200 K to 220 ns at 260 K, corresponding to an Auger limited regime. Indeed, at
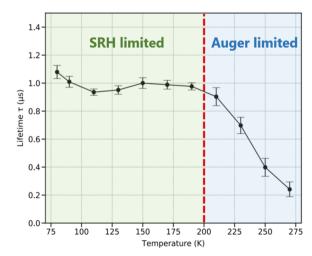

Fig. 2. Minority carrier lifetime measured as a function of temperature, between 77 K and 260 K.

200 K, the intrinsic carrier density is of the same order of magnitude as the non-intentionally doped level of the absorbing layer ($n_i \sim 2 \cdot 10^{15}$ cm^{-3}). Consequently, a high concentration of carriers in the conduction band results in an important Auger recombination rate.

3.2. Optical absorption measurements

Fig. 3 shows the absorption coefficient as a function of wavelength for temperatures ranging from 90 K to 300 K, measured on the authors' test sample structure. The absorption coefficient is deduced from two-step transmission measurements. The first one is performed on the test sample [Fig. 1(a)] since the second one is performed on the only GaSb substrate used for the growth.
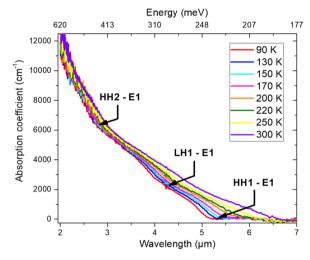

Fig. 3. Absorption coefficient measured on the InAs/InAsSb test sample for different temperatures.

The black arrows in Fig. 3 clearly show different energy transitions of the superlattice at 150 K. The lowest energy transition, corresponding to a transition between the first heavy hole miniband (HH1) to the first electron miniband (E1), allows to reach the energy gap value of the structure: $Eg(150\ K) = 240$ meV. At higher energies, transition from the light hole miniband (LH1) to the electron miniband and transition from the second heavy hole miniband (HH2) to the electron miniband can be observed at 290 meV and 430 meV, respectively. The figure also shows an important red shift of the absorption edge with temperature associated with decreasing energy bandgap of the superlattice with temperature. At 3.4 µm, the absorption coefficient reaches $\alpha = 4800$ cm^{-1} at 150 K. This value seems quite good in comparison with already published values in the literature [10, 15, 16].

The absorption of the light through the sample is then calculated from the measured absorption coefficient and Fig. 4 shows that 76% of the light is absorbed by a 3 µm thick absorbing layer, on a simple pass at 3.4 µm and 150 K. It is assumed that all the generated carriers are collected, meaning that the internal quantum efficiency η_{int} is equal to 1 and that 30% of the light is reflected by the surface. From (3), it is, therefore, possible to estimate the maximum external quantum efficiency value of the structure, with η_{ext} − the external quantum efficiency, R − the reflection at the surface, A − the absorption through the absorbing layer, and η_{int} − the internal quantum efficiency.

$$\eta_{ext} = (1 - R) \cdot A \cdot \eta_{int}. \qquad (3)$$

Thus, a maximum external quantum efficiency close to 53 % can be deduced, corresponding to the state-of-the-art values [4, 17, 18].
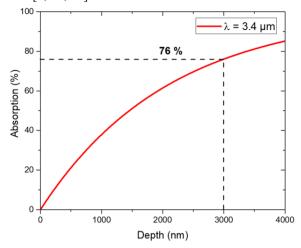

Fig. 4. Light absorption as a function of the absorbing layer thickness calculated from the absorption coefficient at $T = 150$ K and $\lambda = 3.4$ µm.

3.3. External quantum efficiency measurements

The authors are looking now to verify the estimated value of the external quantum efficiency. Thus, a quantum efficiency measurement on the T2SL barrier structure was performed [Fig. 1(b)] using a blackbody source cavity CI Systems SR-200 and a narrow bandpass filter [3 µm; 3.5 µm], more details can be found in Ref. 19**.**

Fig. 5 shows the external quantum efficiency measured at 150 K, with an operating bias of −0.35 V on the barrier device. A value slightly higher than 50% can be observed at 3.4 µm, in perfect accordance with the expected value. This result confirms that the internal quantum efficiency is close to 1, meaning that all the generated carriers are collected. Thus, the minority carrier diffusion length is higher than 3 µm, that is the absorbing layer thickness. To verify this result, the authors are looking now for the minority carrier mobility in the T2SL.
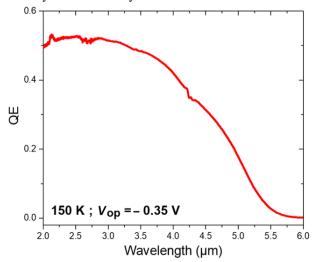

Fig. 5. External quantum efficiency measured on the InAs/InAsSb barrier device at 150 K, for an operating bias of −0.35 V.

3.4. Band structure calculations and Hovel model

Miniband dispersion of the InAs/InAsSb test sample is calculated from an eight-band **k·p** model at 150 K, along the in-plane (x,y) and the growth (z) directions. Parameters of the **k·p** model have been determined from magneto-absorption measurements performed on the test sample at 150 K, all details of the set-up and parameters used for the calculation can be found in Ref. 20.

Fig. 6 shows the electron (E1), first heavy hole (HH1), first light hole (LH1), and second heavy hole (HH2) minibands. The figure illustrates a strong anisotropy of the InAs/InAsSb superlattice structure between the in-plane and growth directions, especially for the HH1 miniband. Indeed, the HH1 miniband is quite dispersive along the in-plane direction while being close to flat along the growth direction, implying a very heavy mass. Heavy hole masses have been extracted from Fig. 6.
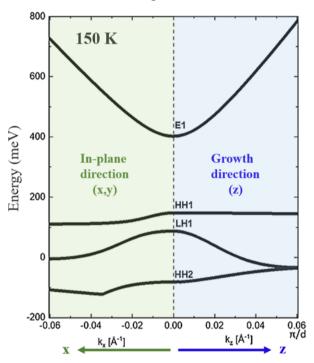

Fig. 6. In-plane (k_x) and growth directions (k_z) miniband dispersion calculated at 150 K from an eight-band **k·p** model, d is the superlattice period. Figure from Krizman *et al.* [20].

$$\begin{cases} m^*_{HH1}(z) = 2.5 \cdot m_0 \\ m^*_{HH1}(x,y) = 0.35 \cdot m_0 \end{cases}. \quad (4)$$

Thus, a heavy hole in-plane value of $0.35 \cdot m_0$, close to the InAs bulk value and a growth-direction value of $2.5 \cdot m_0$ (4) were obtained. This order of magnitude means that the heavy holes are very confined along the growth direction and that the associated mobility is poor. This low vertical mobility should impact the diffusion length and the collection of carriers.

The Hovel model was used to theoretically calculate the external quantum efficiency and extract the minority carrier diffusion length and mobility associated. The Hovel's model, described in more detail in Ref. 19, depends on a few parameters

- absorption coefficient, already measured,
- reflection coefficient, calculated from the classical Snell-Descartes law,
- depletion thickness, extracted from our simulation and capacitance-voltage measurements,
- minority carrier diffusion length.

The latter is used as a fitting parameter and can be extracted from the comparison between the experimental value and the theoretical one calculated from the Hovel model.

Fig. 7 shows the comparison between the external quantum efficiency calculated from the Hovel model with the experimental values, at 90 K, 150 K, and 200 K, and their corresponding operating bias. A very good agreement despite the relative simplicity of the model can be observed.

Minority carrier diffusion length used to fit the experimental quantum efficiency is extracted and reported in Fig. 8. A diffusion length value of 3.7 μm is extracted at 150 K, slightly higher than an absorbing layer thickness of 3 μm. This value confirms that all generated carriers are collected. Heavy hole mobility of 10 cm²/Vs at 150 K is then deduced from Hovel diffusion length value and lifetime measurements (2). This very poor mobility
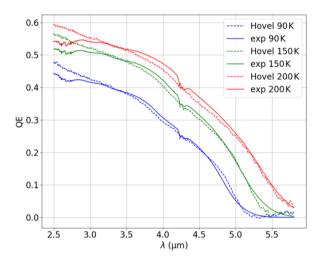

Fig. 7. Comparison of the measured and theoretical (Hovel's model) external quantum efficiency at 90 K, 150 K, and 200 K.
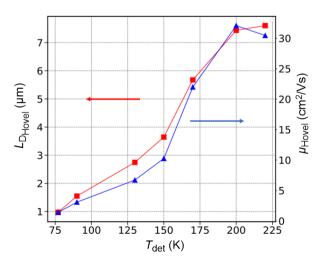

Fig. 8. Minority carrier diffusion length L_{DHovel} and mobility μ_{Hovel} extracted from Hovel model as a function of the temperature.

illustrates the strong confinement of heavy holes within the superlattice. What is more interesting, both diffusion length and mobility continuously increase with temperature, without following the corresponding classical temperature behaviours in $T^{-3/2}$ or $T^{3/2}$. This dependence is related to the minority carrier transport mechanisms involved in the superlattice.

4. Discussion

Two main mechanisms are discussed in the literature [21] and are illustrated schematically in Fig. 9 to describe the mobility. When the wavefunction overlap is important, there is a strong coupling between all quantum wells of the superlattice. In this case, a large energy miniband occurs allowing the transport of all generated carriers through the superlattice structure: it is a miniband transport. Otherwise, if the wavefunction overlap is degraded, due, for example, to a large period superlattice or by the presence of disorder [22], there is no coupling between each quantum well and the miniband cannot be created. The transport is then provided by hopping between discrete energy levels into each quantum well.
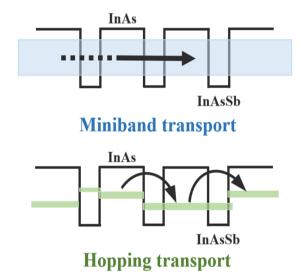

Fig. 9. Schematic diagram of the two main transport mechanisms involved in superlattice. On the top, miniband transport when all the quantum wells are well-coupled. On the bottom, hopping transport through discrete energy level into each quantum well.

In this case, energy is needed to ensure the transport and a strong temperature dependence can be observed [23]. In the temperature range of 77–230 K, the observed temperature dependence of the mobility, as well as the poor mobility values (Fig. 8) suggest a hopping transport through the superlattice. In addition, at $T = 150$ K, the calculated band diagram [20] exhibits a large miniband width of 390 meV for the electron band but a very thin band of 8 meV for the heavy hole band. Following the criteria recently discussed by Klipstein *et al.* [21] and based on Mott theory [24, 25] this thin heavy hole miniband width illustrates a very poor coupling between each quantum well of the superlattice, inducing a hopping transport mechanism.

5. Conclusions

In summary, transport properties of a mid-wave infrared InAs/InAsSb T2SL have been considered to explain significant quantum efficiency value higher than 50% measured at 150 K, despite the high confinement of holes into InAsSb wells. The Hovel model is used to calculate the external quantum efficiency. As a result, minority carrier diffusion length is extracted from the comparison between the experimental value and the Hovel calculation. A diffusion length of 3.7 µm at 150 K is obtained, slightly higher than the absorbing layer, confirming that all generated carriers are collected. Minority carrier mobility is then deduced from the Hovel diffusion length and lifetime measurements. Very poor mobility of 10 cm²/Vs is obtained at 150 K, confirming the strong confinement of holes into InAsSb wells. For both diffusion length and mobility, a continuous increase with temperature was observed. This temperature behaviour is directly related to the transport mechanisms involved in Ga-free superlattices. This strong temperature dependence, as well as low mobility values seem to prove that a hopping transport mechanism occurs between 77 K and 230 K, due to localised states close to the miniband.

Authors' statement

M.B. did the sample fabrication, the electrical characterisation, the study conceptualisation, and analysis and wrote the paper, V.A. did the study conceptualisation, the optical characterisation, and analysis. A.R. did the TRPL measurement, J.-P.P. did the sample growth and supervised the study, I.R-M. supervised the study, N.P-L. supervised the study, and P.C. supervised all the project and study.

References

[1] Kinch, M. A. *Fundamentals of Infrared Detector Materials. TT76.* (SPIE Press, 2007).

[2] Kinch, M. A. *State-of-The-Art Infrared Detector Technology. PM248* (SPIE Press, 2014).

[3] Maimon, S. & Wicks, G. W. nBn detector, an infrared detector with reduced dark current and higher operating temperature. *Appl. Phys. Lett.* **89**, 151109 (2006). https://doi.org/10.1063/1.2360235

[4] Ting, D. Z. *et al.* InAs/InAsSb type-II superlattice mid-wavelength infrared focal plane array with significantly higher operating temperature than InSb. *IEEE Photon. J.* **10**, 1–6 (2018). https://doi.org/10.1109/JPHOT.2018.2877632

[5] Soibel, A. *et al.* Mid-wavelength infrared InAsSb/InAs nBn detectors and FPAs with very low dark current density. *Appl. Phys. Lett.* **114**, 161103 (2019). https://doi.org/10.1063/1.5092342

[6] Olson, B. V. *et al.* Vertical hole transport and carrier localization in InAs/InAs 1−x Sb x type-II superlattice heterojunction bipolar transistors. *Phys. Rev. Appl.* **7**, 024016 (2017). https://doi.org/10.1103/PhysRevApplied.7.024016

[7] Casias, L. K. *et al.* Vertical carrier transport in strain-balanced InAs/InAsSb type-II superlattice material. *Appl. Phys. Lett.* **116**, 182109 (2020). https://doi.org/10.1063/1.5144079

[8] *Handbook Series on Semiconductor Parameters* (Eds. Levinshteĭn, M. E., Rumyantsev, S. L. & Shur, M.) 1–5 (World Scientific, New Jersey, 1996).

[9] Klipstein, P. C. *et al*. Modeling InAs/GaSb and InAs/InAsSb super-lattice infrared setectors. *J. Electron. Mater.* **43**, 2984–2990 (2014). https://doi.org/10.1007/s11664-014-3169-3

[10] Soibel, A. Temperature dependence of diffusion length and mobility in mid-wavelength InAs/InAsSb superlattice infrared detectors. *Appl. Phys. Lett.* **117**, 231103 (2020). https://doi.org/10.1063/5.0027230

[11] Wu, D., Durlin, Q., Dehzangi, A., Zhang, Y. & Razeghi, M. High quantum efficiency mid-wavelength infrared type-II InAs/InAs$_{1-x}$Sb$_x$ superlattice photodiodes grown by metal-organic chemical vapor deposition. *Appl. Phys. Lett.* **114**, 011104 (2019). https://doi.org/10.1063/1.5058714

[12] Zavala-Moran, U. *et al*. Structural, optical and electrical character-izations of midwave infrared Ga-free type-II InAs/InAsSb super-lattice barrier photodetector. *Photonics* **7**, 76 (2020). https://doi.org/10.3390/photonics7030076

[13] Bouschet, M. *et al*. Influence of pixel etching on electrical and electro-optical performances of a Ga-free InAs/InAsSb T2SL barrier photodetector for mid-wave infrared imaging. *Photonics* **8**, 194 (2021). https://doi.org/10.3390/photonics8060194

[14] Arounassalame, V. *et al*. Electro-optical characterizations to study minority carrier transport in Ga-free InAs/InAsSb T2SL XBn midwave infrared photodetector. *Proc. SPIE* **11866**, 1186606 (2021). https://doi.org/10.1117/12.2598159

[15] Webster, P. T., Riordan, N. A., Liu, S., Steenbergen, E. H. & Synowicki, R. A. Absorption properties of type-II InAs/InAsSb superlattices measured by spectroscopic ellipsometry. *Appl. Phys. Lett.* **106**, 6 (2015). https://doi.org/10.1063/1.4908255

[16] Rhiger, D. R. & Smith, E. P. Infrared absorption near the bandgap in the InAs/InAsSb superlattice. *Proc. SPIE* **11503**, 1150305 (2020). https://doi.org/10.1117/12.2569820

[17] Haddadi, A. *et al*. High-performance short-wavelength infrared photodetectors based on type-II InAs/InAs$_{1-x}$Sb$_x$ /AlAs$_{1-x}$ Sb$_x$ superlattices. *Appl. Phys. Lett.* **107**, 141104 (2015). https://doi.org/10.1063/1.4932518

[18] Ariyawansa, G., Duran, J., Reyner, C. & Scheihing, J. InAs/InAsSb Strained-layer superlattice mid-wavelength infrared detector for high-temperature operation. *Micromachines* **10**, 806 (2019). https://doi.org/10.3390/mi10120806

[19] Arounassalame, V. *et al*. Anisotropic transport investigation through different etching depths in InAs/InAsSb T2SL barrier midwave infrared detector. *Infrared Phys. Technol.* **126**, 104315 (2022). https://doi.org/10.1016/j.infrared.2022.104315

[20] Krizman, G. *et al*. Magneto-spectroscopy investigation of InAs/InAsSb superlattices for midwave infrared detection. *J. Appl. Phys.* **130**, 055704 (2021). https://doi.org/10.1063/5.0054320

[21] Klipstein, P. C. Perspective on III–V barrier detectors. *Appl. Phys. Lett.* **120**, 060502 (2022). https://doi.org/10.1063/5.0084100

[22] Bellotti, E. Disorder-induced degradation of vertical carrier transport in strain-balanced antimony-based superlattices. *Phys. Rev. Appl.* **16**, 054028 (2021). https://doi.org/10.1103/PhysRevApplied.16.054028

[23] Mott, N. F. Conduction in non-crystalline materials: III. Localized states in a pseudogap and near extremities of conduction and valence bands. *Philos. Mag.* **19**, 835–852 (1969). https://doi.org/10.1080/14786436908216338

[24] Mott, N. F. On the transition to metallic conduction in semiconductors. *Can. J. Phys.* **34**, 1356–1368 (1956). https://doi.org/10.1139/p56-151

[25] Mott, N. F. Electrons in disordered structures. *Adv. Phys.* **16**, 49–144 (1967). https://doi.org/10.1080/00018736700101265